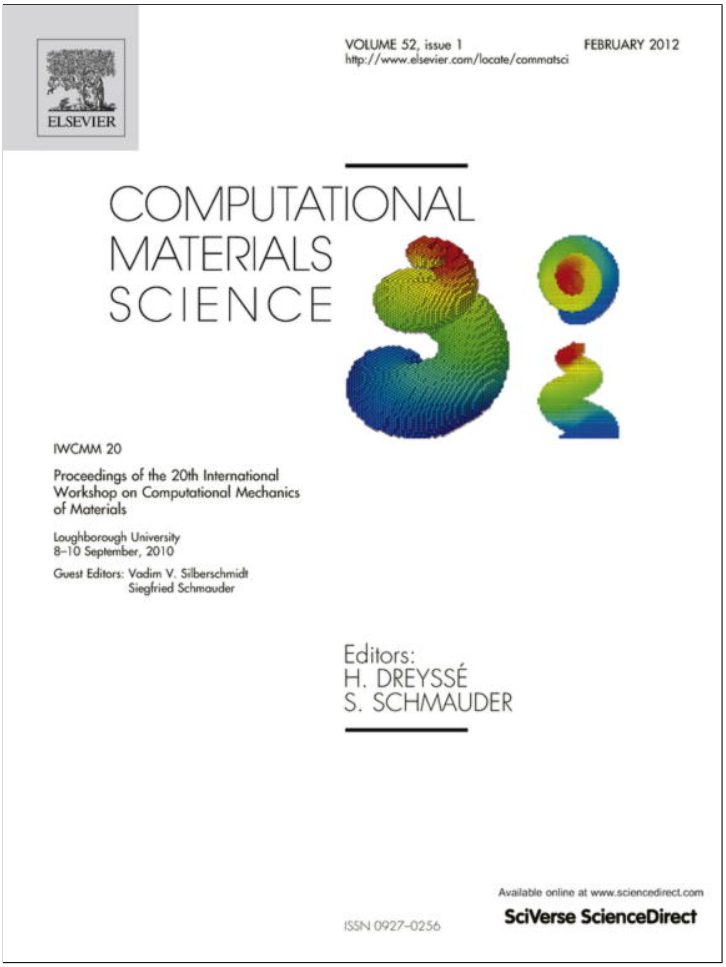

Computational Materials Science 52 (2012) 7–13

Contents lists available at ScienceDirect

Computational Materials Science

journal homepage: www.elsevier.com/locate/commatsci

Grain size effects on plastic strain and dislocation density tensor fields in metal polycrystals

N.M. Cordero [a], S. Forest [a,*], E.P. Busso [a], S. Berbenni [b,c], M. Cherkaoui [c]

[a] MINES ParisTech, Centre des Matériaux, CNRS UMR 7633, BP 87 91003 Evry Cedex, France
[b] Arts et Métiers ParisTech, Metz Technopole, Laboratoire d'Etude des Microstructures et de Mécanique des Matériaux, CNRS UMR 7239, 57078 Metz, France
[c] Georgia Tech Lorraine, GT-CNRS UMI 2958, 57070 Metz, France

ARTICLE INFO

Article history:
Received 31 October 2010
Received in revised form 25 February 2011
Accepted 27 February 2011
Available online 12 April 2011

ABSTRACT

A strain gradient crystal plasticity model is used to explore the grain size effect on the fields of plastic strain and of the dislocation density tensors in two-dimensional polycrystals. Finite element simulations are performed for several aggregates of 24 and 52 grains with a detailed description of the intragranular fields. It is found that the increasing energy cost associated with the development of geometrically necessary dislocations (GNDs) leads to the formation of a network of intense slip bands accommodating the imposed deformation in ultra-fine grain polycrystals.

1. Introduction

The behaviour of a polycrystalline material is notably dependent on grain size. Finite element simulations of polycrystals based on classical continuum crystal plasticity do not account for this dependence so that the predicted macroscopic response as well as the predicted fields inside the aggregates are size independent [22,3,27]. As it would be irrelevant to enter the grain size into the constitutive model explicitly, its effects should arise from the gradient fields. The dislocation density tensor [23] characterising the plastic deformation incompatibility is directly related to the plastic strain gradient and therefore is a possible way to induce strain gradient effects in continuum crystal plasticity simulations.

Finite element simulations based on strain gradient plasticity models are quite seldom in the literature. They can be classified in two main groups. The first group of models computes the dislocation density tensor or geometrically necessary dislocation (GND) densities from the gradients of the plastic strain field at each time increment and do not introduce higher order stresses nor additional boundary conditions [1,7,9]. In the second group of models [19,5,12], higher order stress tensors are introduced to compute the power expenditure associated with the rate of the dislocation density tensor. Such generalised continuum theories also include additional interface conditions at grain boundaries like continuity of plastic strain or of some dislocation densities in addition to the continuity of displacement. Some finite element simulations on a limited number of grains are provided in [16,5,4]. However, due to the high non-linearity of the models and the number of additional degrees of freedom, only coarse meshes were used so that only a poor description of the gradient fields is given.

Most contributions were dedicated to the prediction of the grain size-dependent overall response of polycrystals and to the derivation of Hall–Petch-type relationships. In the present work, we want to show how the grain size also affects the intragranular fields of plastic strains and of the dislocation density tensor. For that purpose, a generalised continuum model closely related to strain gradient plasticity theories is implemented. The *microcurl* model is a micromorphic crystal plasticity model belonging to the class of generalised continuum models with additional degrees of freedom as presented in [13,15]. It was proposed in [12] to regularise the response of a strain gradient plasticity theory including the full curl of the plastic deformation tensor $\boldsymbol{H}^p$ [19] in the presence of interfaces. In the present work, finer finite element meshes than in previous contributions are used so that the fields can be described properly. However, the analysis is limited to the 2D case.

In Section 2, the *microcurl* model is introduced for crystal plasticity. The role of continuity requirements at grain boundaries is discussed in Section 3. Finite element simulations of the simple shear response of several random idealised aluminium aggregates are performed for various grain sizes in Section 4. The dependence of the overall response and of the plastic strain and dislocation density tensor fields on the grain size are then shown.

The following notation is used: vectors and second-rank tensors are respectively denoted by $\underset{\sim}{\boldsymbol{a}}$ and $\boldsymbol{a}$; the curl operator in a Cartesian frame for a tensor $\underset{\sim}{\boldsymbol{a}}$ of rank two is

$$(\mathrm{curl}\ \underset{\sim}{\boldsymbol{a}})_{ij} = \epsilon_{jkl} a_{ik,l}, \tag{1}$$

where ϵ_{ijk} is the permutation tensor.

* Corresponding author. Tel.: +33 1 60 76 30 51; fax: +33 1 60 76 31 50.
E-mail addresses: samuel.forest@ensmp.fr, samuel.forest@mines-paristech.fr (S. Forest).

0927-0256/$ - see front matter © 2011 Elsevier B.V. All rights reserved.
doi:10.1016/j.commatsci.2011.02.043

2. The *microcurl* model for crystal plasticity

In the crystal plasticity theory for small deformations, the gradient of the velocity field, $\dot{\underline{u}}$, can be decomposed into the elastic and plastic deformation rates:

$$\dot{\underset{\sim}{H}} = \dot{\underline{u}} \otimes \nabla = \dot{\underset{\sim}{H}}^e + \dot{\underset{\sim}{H}}^p, \quad \text{where} \quad \dot{\underset{\sim}{H}}^p = \sum_{\alpha}^{N} \dot{\gamma}^\alpha \underline{l}^\alpha \otimes \underline{n}^\alpha, \tag{2}$$

with N the number of slip systems, $\dot{\gamma}^\alpha$ the slip rate for the slip system α, $\underline{l}^\alpha$ the slip direction and $\underline{n}^\alpha$ the normal to the slip plane. The elastic deformation, $\underset{\sim}{H}^e$, accommodates the incompatibilities induced by the plastic deformation field, $\underset{\sim}{H}^p$. Applying the curl operator to a compatible field gives zero, so we have:

$$\operatorname{curl} \dot{\underset{\sim}{H}} = \operatorname{curl} \dot{\underset{\sim}{H}}^e + \operatorname{curl} \dot{\underset{\sim}{H}}^p = 0. \tag{3}$$

The incompatibility of plastic deformation is characterised by the dislocation density tensor [23,8], defined as:

$$\underset{\sim}{\Gamma} = -\operatorname{curl} \underset{\sim}{H}^p = \operatorname{curl} \underset{\sim}{H}^e. \tag{4}$$

The *microcurl* model, like similar strain gradient plasticity models, includes the dislocation density tensor into the continuum crystal plasticity framework. It produces a size-dependent linear kinematic hardening coming from a back-stress contribution from the dislocation density tensor, i.e., from GNDs. Two generalised moduli, introduced as material parameters, control the main characteristics of the generated size effects: the maximum extra-hardening, the characteristic size for which size effects occur and the scaling law exponent.

2.1. Balance equations

The independent degrees of freedom of the theory are the displacement vector, $\underline{u}$, and the generally non-symmetric second-rank plastic micro-deformation tensor, $\underset{\sim}{\chi}^p$. The components of $\underset{\sim}{\chi}^p$ are introduced as independent degrees of freedom and are in general distinct from the components of $\underset{\sim}{H}^p$, still treated as internal variable. The definition of Eq. (4) motivates the use of a first gradient theory with respect to the degrees of freedom in which only the curl of the plastic micro-deformation gradient is assumed to have an effect in the power of internal forces.

The *microcurl* continuum is therefore characterised by an enhanced power density of internal forces of the form:

$$p^{(i)} = \underset{\sim}{\sigma} : \dot{\underset{\sim}{H}} + \underset{\sim}{s} : \dot{\underset{\sim}{\chi}}^p + \underset{\sim}{M} : \operatorname{curl} \dot{\underset{\sim}{\chi}}^p. \tag{5}$$

The stress tensor, $\underset{\sim}{\sigma}$, is symmetric while the micro-stress tensor, $\underset{\sim}{s}$, and the double-stress tensor, $\underset{\sim}{M}$, are generally not symmetric. The method of virtual power is used to derive the generalised balance of momentum equations. In the absence of body forces, we have:

$$\operatorname{div} \underset{\sim}{\sigma} = 0, \quad \operatorname{curl} \underset{\sim}{M} + \underset{\sim}{s} = 0. \tag{6}$$

The corresponding boundary conditions are,

$$\underline{t} = \underset{\sim}{\sigma} \cdot \underline{n}, \quad \underset{\sim}{m} = \underset{\sim}{M} \cdot \underset{\approx}{\epsilon} \cdot \underline{n}, \tag{7}$$

where $\underline{t}$ and $\underset{\sim}{m}$ are the simple and double tractions at the boundary, $\underline{n}$ is the unit normal vector to the boundary and $\underset{\approx}{\epsilon}$ is the permutation tensor.

2.2. Constitutive equations

The free energy function is assumed to have the following arguments:

$$\psi\left(\underset{\sim}{\varepsilon}^e, \quad \underset{\sim}{e}^p := \underset{\sim}{H}^p - \underset{\sim}{\chi}^p, \quad \underset{\sim}{\Gamma}_\chi := \operatorname{curl} \underset{\sim}{\chi}^p\right), \tag{8}$$

where $\underset{\sim}{e}^p$ is the relative plastic strain measuring the difference between the plastic deformation and the plastic micro-deformation. $\underset{\sim}{\Gamma}_\chi$ is the curl of $\underset{\sim}{\chi}^p$ in the same way as the dislocation density tensor given in Eq. (4) is the curl of $\underset{\sim}{H}^p$. The following state laws are adopted:

$$\underset{\sim}{\sigma} = \rho \frac{\partial \psi}{\partial \underset{\sim}{\varepsilon}^e}, \quad \underset{\sim}{s} = -\rho \frac{\partial \psi}{\partial \underset{\sim}{e}^p}, \quad \underset{\sim}{M} = \rho \frac{\partial \psi}{\partial \underset{\sim}{\Gamma}_\chi}, \tag{9}$$

so that the residual intrinsic dissipation rate remains as

$$D = (\underset{\sim}{\sigma} + \underset{\sim}{s}) : \dot{\underset{\sim}{H}}^p = \sum_{\alpha=1}^{N} (\tau^\alpha + \underset{\sim}{s} : (\underline{l}^\alpha \otimes \underline{n}^\alpha)) \dot{\gamma} \geqslant 0. \tag{10}$$

A viscoplastic potential expressed in terms of the effective stress, $\Omega(\underset{\sim}{\sigma} + \underset{\sim}{s})$, is introduced such that the flow rule reads:

$$\dot{\underset{\sim}{H}}^p = \frac{\partial \Omega}{\partial (\underset{\sim}{\sigma} + \underset{\sim}{s})}. \tag{11}$$

Assuming a quadratic potential in Eq. (9), the following linear relationships are obtained:

$$\underset{\sim}{\sigma} = \underset{\approx}{\Lambda} : \underset{\sim}{\varepsilon}^e, \quad \underset{\sim}{s} = -H_\chi \underset{\sim}{e}^p, \quad \underset{\sim}{M} = A \underset{\sim}{\Gamma}_\chi, \tag{12}$$

where $\underset{\approx}{\Lambda}$ is the four-rank tensor of the elastic moduli assumed isotropic in this work, H_χ and A are the generalised moduli. A generalised Schmid criterion is adopted

$$f^\alpha(\underset{\sim}{\sigma}, \underset{\sim}{s}) = |\tau^\alpha + \underset{\sim}{s} : (\underline{l}^\alpha \otimes \underline{n}^\alpha)| - \tau_c^\alpha,$$
$$\Omega(\underset{\sim}{\sigma}, \underset{\sim}{s}) = \frac{K}{n+1} \sum_{\alpha=1}^{N} \left\langle \frac{f^\alpha(\underset{\sim}{\sigma}, \underset{\sim}{s})}{K} \right\rangle^{n+1}, \tag{13}$$

where τ_c^α is the critical resolved shear stress. K and n are viscosity parameters that are chosen here in such a way that no strain-rate effect is noticeable for the investigated rates. A back-stress component naturally arises in the yield function by combining Eqs. (6) and (12):

$$x^\alpha = -\underset{\sim}{s} : (\underline{l}^\alpha \otimes \underline{n}^\alpha) = A(\operatorname{curl} \operatorname{curl} \underset{\sim}{\chi}^p) : (\underline{l}^\alpha \otimes \underline{n}^\alpha). \tag{14}$$

The modulus H_χ in Eq. (12) sets a coupling between $\underset{\sim}{\chi}^p$ and $\underset{\sim}{H}^p$. It can be interpreted as a penalty factor enforcing the relative plastic deformation, $\underset{\sim}{e}^p$, to remain sufficiently small. Then, high values of the coupling modulus, H_χ, enforce the plastic micro-deformation to be as close as possible to the macroscopic plastic deformation, $\underset{\sim}{H}^p$. Due to Eq. (8), this internal constraint also links $\underset{\sim}{\Gamma}_\chi$ and the dislocation density tensor $\underset{\sim}{\Gamma}$. In what follows, as H_χ will remain high enough, $\underset{\sim}{\Gamma}_\chi$ is computed and referred to as the dislocation density tensor. Moreover, as shown in [12], H_χ has a major effect on the scaling law exponent. In the limit of very high values of H_χ, we have $\underset{\sim}{\chi}^p \equiv \underset{\sim}{H}^p$ so that the *microcurl* model is equivalent to more conventional strain gradient plasticity according to [19].

3. Size effects induced by grain boundaries

The *microcurl* model is now applied to simulate the response of polycrystalline aggregates and the effects of their microstructure's size. Size effects in polycrystals are strongly dependent on the conditions at grain boundaries. Physically motivated interface conditions exist in the literature (see, for instance, [20]). However, in the present work no special interface law is set and we only consider the interface conditions that arise from the formulation of

the balance equations of the continuum model. These conditions are the continuity of displacement, $\underline{\boldsymbol{u}}$, and of the plastic micro-deformation, $\boldsymbol{\chi}^p$, on the one hand, and the continuity of the simple and double tractions $\underline{\boldsymbol{t}}$ and $\boldsymbol{m}$ given in Eq. (7), on the other hand, across a grain boundary. In contrast, the plastic deformation $\boldsymbol{H}^p$ is generally not continuous at an interface. However, for high values of parameter H_χ, $\boldsymbol{H}^p$ almost coincides with $\boldsymbol{\chi}^p$ so that it is practically continuous at a grain boundary. This corresponds to the internal constraint introduced at the end of Section 2.2. The continuity of the associated tractions expresses the transmission of classical and generalised internal forces from one grain to another through grain boundaries. In that way, such continuum models are then able to mimic the development of dislocation pileups at grain boundaries [18].

The size effects exhibited by the solution of the boundary value problem are linked to an intrinsic length scale, l_s, introduced through the generalised moduli H_χ and A of Eq. (12) as:

$$l_s = \sqrt{\frac{A}{H_\chi}}. \tag{15}$$

This intrinsic length scale has to be consistent with the fact that plasticity effects occur at scales ranging from hundreds of nanometres to a few microns. In addition, as presented in Section 2.2, the coupling modulus, H_χ, has to be chosen high enough to ensure that $\boldsymbol{\chi}^p$ and $\boldsymbol{H}^p$ are close. These requirements are guidelines for the choice of relevant generalised moduli H_χ and A. The set of material parameters used in this paper (see Table 1) has been chosen in that way. It corresponds to an idealised aluminium alloy for large grains but no quantitative agreement with experimental results was sought for, due to the crystallographic simplifications in the simulations.

The finite element simulations are performed on periodic two-dimensional (2D) meshes of periodic polycrystalline aggregates randomly generated by a method based on Voronoï tessellations. Quadratic elements are used with two displacements and four micro-deformation degrees of freedom per node. The largest mesh considered contains 77,778 degrees of freedom. Note that the finite element discretisation was chosen fine enough to ensure accurate and mesh size independent results. By extension, the relative mesh size compared to the intrinsic length scale, l_s, has no impact on the results. An example of a microstructure is shown in Fig. 1. The grains are represented by Voronoï polyhedra, the distribution of their centres is controlled in such a way that the microstructure is characterised by a mean grain size, d. Various mean grain sizes, d, ranging from tens of nanometres to hundreds of microns, are investigated. Random orientations are assigned to the grains and two slip systems are taken into account. In 2D, the plastic behaviour of f.c.c. crystals can be simulated with 2D planar double slip by considering two effective slip systems separated by an angle of 2ϕ with $\phi = 35.1°$ [2,6]. The overall response of the polycrystal is predicted using periodic homogenisation for generalised continua [17]. The displacement field is assumed to be of the form

$$\underline{\boldsymbol{u}}(\underline{\boldsymbol{x}}) = \underset{\sim}{\boldsymbol{E}} \cdot \underline{\boldsymbol{x}} + \underline{\boldsymbol{v}}(\underline{\boldsymbol{x}}), \tag{16}$$

with $\underline{\boldsymbol{v}}$ a periodic fluctuation, which means that it takes identical values at homologous points of the unit cell. The imposed average strain tensor is $\boldsymbol{E}$. Periodicity is also assumed for the plastic micro-deformation field, $\underset{\sim}{\boldsymbol{\chi}}^p$, which implies that no curl of the

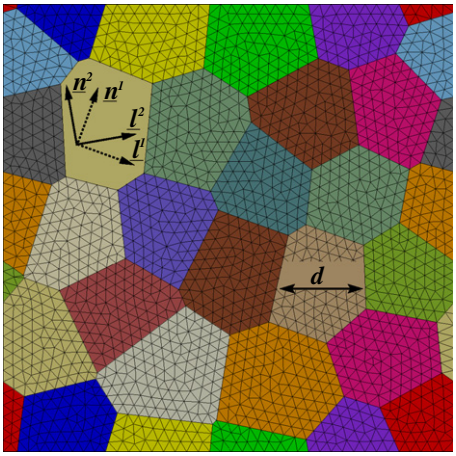

Fig. 1. Example of periodic mesh of the 2D periodic aggregates used in the finite element simulations.

macroscopic plastic deformation is imposed on the unit cell. According to periodic homogenisation, the simple and double tractions $\underline{\boldsymbol{t}}$ and $\boldsymbol{m}$ are anti-periodic at homologous points of the unit cell.

As polycrystals are random materials, the periodicity constraint may induce a bias in the estimation of the effective properties for rather small numbers of grains. In order to minimise this boundary effect, we have to consider several realisations of the microstructure and to perform ensemble averaging [29]. For that purpose, three aggregates of 24 grains and a larger one of 52 grains are studied. A better statistics would require a larger number of realisations but it will be seen that reasonable estimates are obtained in the present case. Morphology and individual grain orientations are different for each sample.

4. Grain size effects in polycrystalline aggregates

4.1. Overall response

Finite element simulations of the boundary value problem presented previously have been conducted under generalised plane strain conditions on the considered aggregates of idealised aluminium. Isotropic hardening is introduced as in [21] to obtain a realistic response of large aluminium grains. A simple size independent hardening law is chosen:

$$\tau_c^\alpha = \tau_c + Q \sum_{\beta=1}^{N} h^{\alpha\beta} \left(1 - \exp\left(-b\gamma_{\text{cum}}^\beta\right)\right), \tag{17}$$

where Q and b are material parameters defining non-linear isotropic hardening, $h^{\alpha\beta}$ is the interaction matrix and $\gamma_{\text{cum}}^\beta$ is the accumulated plastic slip on the slip system β. The accumulated plastic slip results from the integration of the differential equation $\dot{\gamma}_{\text{cum}}^\beta = |\dot{\gamma}^\beta|$. Table 1 gives the material parameters used in the simulations. They have been chosen to obtain an acceptable description of aluminium aggregates with large microstructures and to set a consistent intrinsic length scale $l_s = 0.1$ μm. In this paper we do not calibrate the amplitude of the extra-hardening and the scaling law exponent from experimental results, only one set of material parameters

Table 1
Set of material parameters used in the finite element simulations.

μ (MPa)	τ_c (MPa)	Q (MPa)	b	$h^{\alpha\alpha}$	$h^{\alpha\beta,\alpha\neq\beta}$	H_χ (MPa)	A (MPa mm^2)	l_s (μm)
27,000	0.75	7.9	10.2	1	4.4	1.0×10^6	1.0×10^{-2}	1.0×10^{-1}

was investigated. The macroscopic stress–strain curves presented in Fig. 2 give the averaged stress–strain response of the four aggregates introduced in the previous section. They are obtained by applying a simple shear loading controlled by the mean strain component $E_{12} = \langle \varepsilon_{12} \rangle$, where $\langle\rangle$ denotes volume averaging over the polycrystal unit cell, on the aggregates with various grain sizes d taken in the size-dependent domain. The mean stress component $\Sigma_{12} = \langle \sigma_{12} \rangle$ is then computed from the finite element results. The curves show that the kinematic hardening produced by the model is strongly size-dependent and increases for smaller grains. This linear kinematic hardening is quite ideal and leads to values of Σ_{12} that may be surprisingly high. In future work, the constitutive framework has to be extended to include non-linear kinematic hardening. However, some experimental data available in the literature show that very high values of the mean stress can be reached with fine grain sizes [26,28]. Fig. 3 shows the effect of the mean grain size, d, on the macroscopic flow stress at 1% plastic strain in a log–log diagram. The solid curve is the mean curve obtained with the 24-grain aggregates, the error bars represent the standard deviation. The dashed curve is obtained with the larger aggregate of 52 grains. Both curves have a *tanh*-shape with two saturation plateaus when the grain size, d, is larger than 20 μm and smaller than 0.1 μm and a transition domain for intermediate sizes. When d is large compared to the intrinsic length scale, l_s, strain gradient effects are small and the kinematic hardening arising from the *microcurl* model vanishes. The model saturates when d is of the order of l_s or smaller. A strong size dependence is observed in the transition domain, the polycrystals becoming harder for smaller microstructures. The position of the transition zone, the maximum extra-stress (the distance between the two plateaus) and the scaling law exponent, m, in the size dependent domain are controlled by the material parameters used in the model. The scaling law exponent is defined as the slope in the log–log diagram in the size-dependent domain, reflecting the scaling law:

$$\Sigma_{12} \propto d^m. \tag{18}$$

A detailed parameter study is done in [12] in the case of two-phase microstructures. It is shown in particular that m is controlled by the coupling modulus, H_χ, and that values ranging from $m = 0$ to $m = -2$ can be simulated with the *microcurl* model. In the present work, we obtain $m = -0.76$ and $m = -0.78$ for polycrystals, which are a bit higher compared to the ideal Hall–Petch scaling law exponent $m = -0.5$. This means that the chosen value for the generalised modulus H_χ has to be re-calibrated. Such a calibration has been done in [11] to obtain $m = -0.5$ but it is not presented here. The

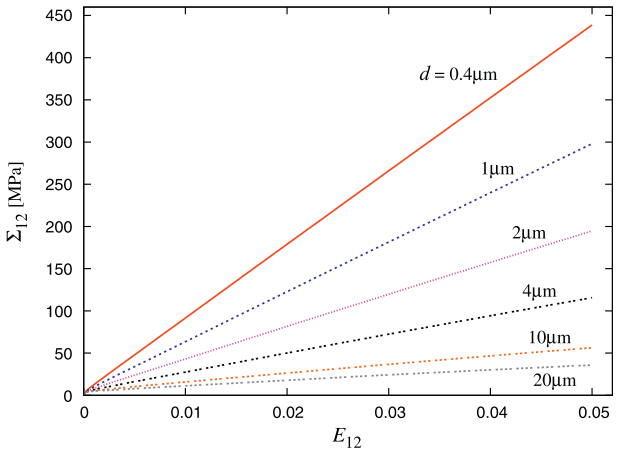

Fig. 2. Averaged macroscopic stress–strain response of the considered aggregates of 24 and 52 grains under simple shear for various mean grain sizes, d.

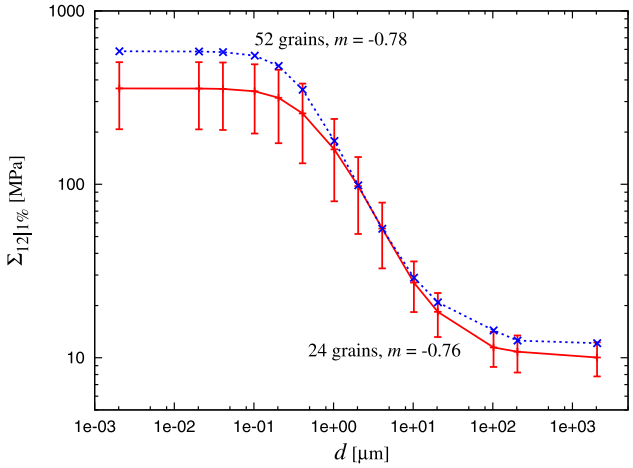

Fig. 3. Effect of the mean grain size, d, on the macroscopic flow stress $\Sigma_{12|1\%}$ at 1% accumulated plastic slip. The results are obtained with three 24-grain aggregates and with one 52-grain aggregate under simple shear for the material parameters given in Table 1. The solid curve is the average curve obtained with the 24-grain aggregates, the error bars give the standard deviation. The corresponding scaling law exponent, m, is identified for each case.

curves of Fig. 3 show that the various realisations of the polycrystal lead to rather close stress responses, especially in the size-dependent domain.

The saturation that occurs for small microstructures is not observed with conventional strain gradient plasticity models. Instead, the stress increases infinitely for vanishingly small grain sizes [12]. However, such continuum crystal plasticity models are not expected to be relevant for nano-grains since they assume the existence of a sufficiently high density of dislocation sources. In particular the present model does not account for the inverse Hall–Petch behaviour, i.e, the yield stress decreases for grain sizes below a critical size, that such materials exhibit [10].

4.2. Fields of accumulated plastic slip

Grain size effects are not limited to the overall response of polycrystals. It also affects the intragranular mechanical fields. Fig. 4 shows the contour plots of the accumulated plastic slip field, computed as

$$\dot{p} = \sqrt{\frac{2}{3}\dot{\underset{\sim}{\varepsilon}}^p : \dot{\underset{\sim}{\varepsilon}}^p}, \tag{19}$$

where the plastic strain $\boldsymbol{\varepsilon}^p$ is the symmetric part of the plastic deformation, $\boldsymbol{H}^p$. In order to catch the details of this field and to understand how it evolves with the grain size, its distribution is given in Fig. 6a in the form of histograms. These histograms are obtained for each grain size by including the simulated distributions of p for all the considered realisations. The plotted frequency represents the fraction of the integration points, where the accumulated plastic slip takes a value inside the interval $p \pm \Delta p$ with $2\Delta p = 0.001$. Between 11,000 and 19,000 integration points are contained in each mesh, allowing a fairly fine description of the field. One can see that the obtained curves are not bell-shaped and therefore the distributions are not Gaussian. Instead, the curves present an early peak centered at $p^{peak} \approx 0.005$, at half the imposed overall value of p. When the grains are smaller, the value of p^{peak} is smaller and the peak is higher. The peak is followed by a long tail which becomes longer with smaller d.

The contour plots and distributions are presented for the same overall value, $\langle p \rangle$, fixed at 1% so that we can compare the different cases and visualise directly the fields and their corresponding

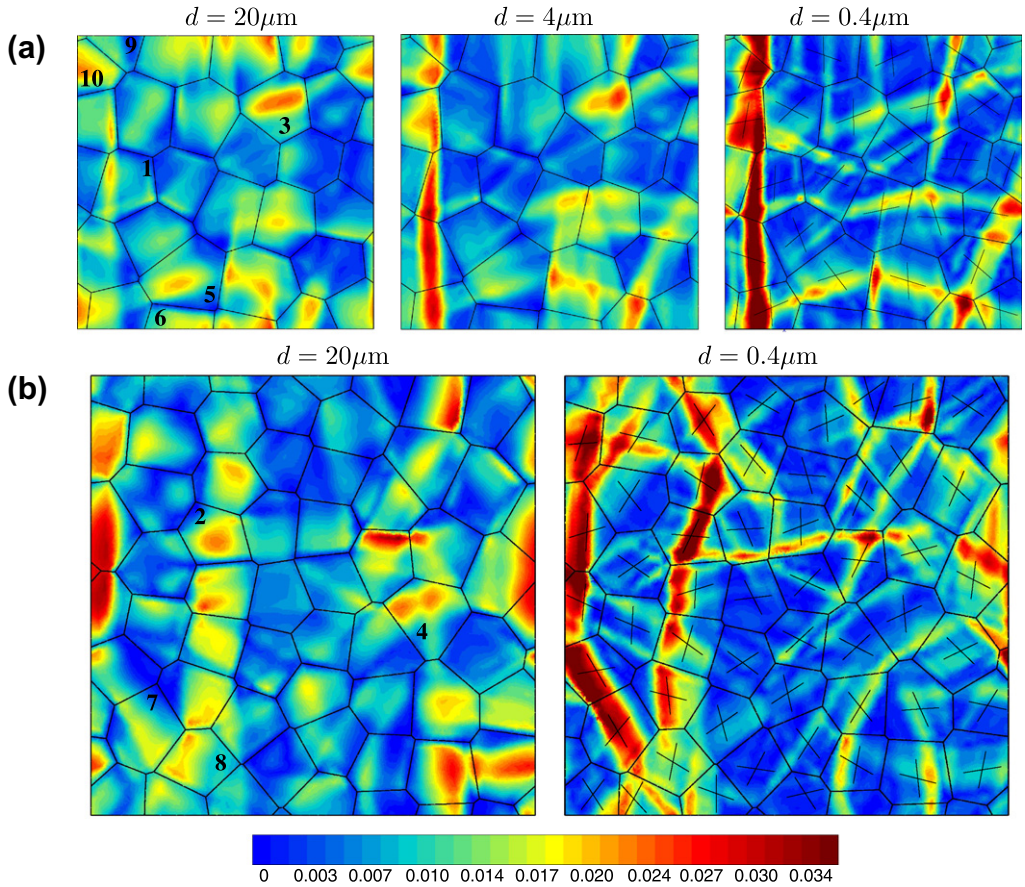

Fig. 4. Effect of the mean grain size, d, on the accumulated plastic slip, p. These contour plots are obtained with (a) the 24-grain aggregate of Fig. 1 and (b) the 52-grain aggregate under simple shear for the same overall value $\langle p \rangle = 0.01$. The pairs of slip plane directions are represented on the 0.4 μm contour plots.

distributions. A clear dependence of the field of accumulated plastic slip, p, on the grain size can be seen in Fig. 4. For $d = 20\ \mu m \gg l_s$, at the very beginning of the size dependent domain according to Fig. 3, the following observations can be made. Deformation bands appear in some grains, e.g., grains 1, 2, 3 and 4. In these grains, p reaches values more than twice the mean value (0.0208, 0.0232, 0.0243 and 0.0238 in grains 1, 2, 3 and 4 respectively). In the grains without such highly deformed zones, p is approximately ranging from 0.0005 to 0.0168 for a mean value of 0.0091 close to $\langle p \rangle$. When d is smaller, $20\ \mu m \geqslant d \geqslant 0.4\ \mu m \approx l_s$, significant evolutions happen:

- The deformation bands initiated in some large grains, e.g., 1 and 2, intensify and propagate in neighbouring grains. A network of strain localisation bands is progressively built across the microstructure. These bands are slip bands since they are parallel to the slip directions represented on the 0.4 μm contour plots of Fig. 4.
- In parallel, the low deformed zones of the grains exhibiting slip bands grow and get less deformed as the slip bands intensify. For $d = 20\ \mu m$, the accumulated plastic slip in the grains 1 and 2 was $0.0010 \leqslant p \leqslant 0.0208$ and $0.0004 \leqslant p \leqslant 0.0232$ respectively, it becomes $0.0004 \leqslant p \leqslant 0.0502$ and $0.0002 \leqslant p \leqslant 0.0492$ with $d = 0.4\ \mu m$. In the grains with no slip band, p is approximately ranging from 0.0002 to 0.0209 for a mean value of 0.0051
- In other grains, a slip band observed along a slip direction in a large grain can vanish in favor of a new slip band along the other slip direction when d is smaller. This is observed, for example, in grain 3.
- A last situation is noticed, e.g. in grain 4, where the slip band formed for $d = 20\ \mu m$ vanishes in smaller microstructures. Here, the accumulated plastic slip goes from $0.0025 \leqslant p \leqslant 0.0238$ to $0.0005 \leqslant p \leqslant 0.0170$ when d decreases from 20 μm to 0.4 μm.

To sum up, when the grain size gets smaller, a network of slip bands is progressively built. These bands compensate the larger low deformed zones, where probably, the plastic strain cannot develop any more due to the higher energy cost associated with its gradient. In smaller grains, the plastic strain becomes larger inside the bands. This is a result of the fact that the contour plots are obtained with a fixed mean accumulated plastic slip implying a higher applied overall strain and stress for small grain sizes.

These observations are consistent with the histograms of Fig. 6a. Indeed, the distributions exhibit a slightly higher peak centered at smaller values of p when the grains are smaller. That is to say, the distribution of p becomes more homogeneous in most grains and the weakly deformed zones increase. At the same time, smaller grains lead to a longer tail of the distribution denoting that p is locally higher, as observed in the localisation bands.

4.3. Grain size effect on the dislocation density tensor field

The evolution of the dislocation density field is studied in the same way as in the previous section. The dislocation density tensor can be related to the lattice curvature by means of Nye's formula. Lattice curvature can be measured experimentally with EBSD 2D misorientation mapping [24]. The components of the dislocation density tensors can also be decomposed in terms of the so-called

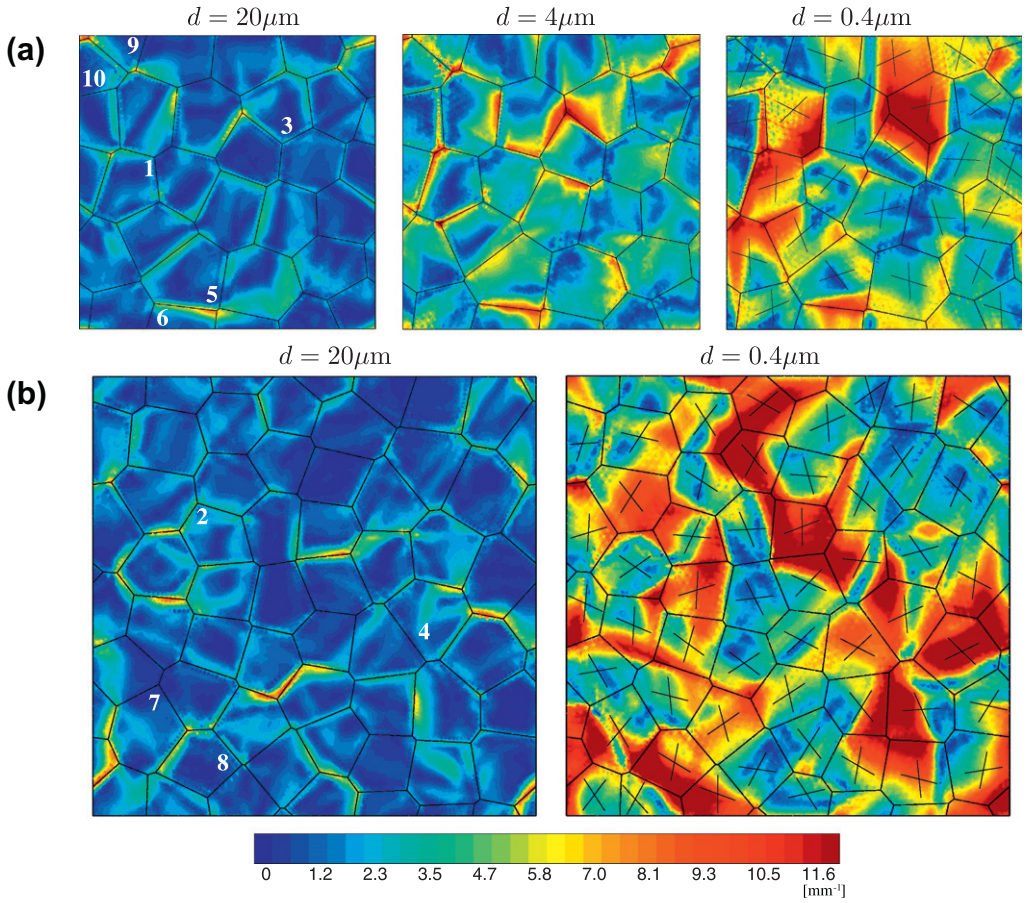

Fig. 5. Effect of the mean grain size, d, on the norm of the dislocation density tensor, Γ. These contour plots are obtained with (a) the 24-grain aggregate of Fig. 1 and (b) the 52-grain aggregate under simple shear for the same overall value $\langle p \rangle = 0.01$. The pairs of slip plane directions are represented on the 0.4 μm contour plots.

geometrically necessary dislocation densities associated to the two slip systems considered in this work. However, for the sake of brevity, we will consider only the field of the norm of the dislocation density tensor which is defined as

$$\Gamma = \sqrt{\underset{\sim}{\Gamma} : \underset{\sim}{\Gamma}} \tag{20}$$

and combines all present GNDs. Fig. 5 shows the contour plots of the norm Γ of the dislocation density tensor. The physical dimension of Γ in the contour plots is mm^{-1}. Fig. 6b describes its distributions for various grain sizes. Γ is stored at all integration points, the plotted frequency represents the fraction of these points, where Γ takes a value inside the interval $\Gamma \pm \Delta\Gamma$ with $2\Delta\Gamma = 0.25$ mm^{-1}. Again, the obtained distributions are not Gaussian, they also present a strong dependence on the grain size and their evolution is very different from what was obtained for the plastic strain (Fig. 6a). Decreasing peaks and longer tails are observed for smaller grains. The contour plots and distributions are still obtained with the overall value of p fixed at 1%. For $d = 20\ \mu\text{m} \gg l_s$, one can observe that:

- Γ is localised at the grain boundaries and almost vanishes in the grain cores. See for example Grains 5 and 6 or 7 and 8 in Fig. 5. For the first pair, $\Gamma = 6.75$ mm^{-1} at the grain boundary and $\Gamma = 0.10$ and 0.64 mm^{-1} at the centres of Grains 5 and 6 respectively. $\Gamma = 5.98$ mm^{-1} at the boundary between 7 and 8, $\Gamma = 1.34$ and 0.10 mm^{-1} at their centres.
- The GND pileups appear at most grain boundaries; their existence, shape and intensity depend notably on the relative orientations of the considered grains.

When d is smaller, $20\ \mu\text{m} \geqslant d \geqslant 0.4\ \mu\text{m} \approx l_s$, the following changes happen:

- The highest values of Γ are still reached close to the grain boundaries.
- The GND pileups spreads over the grain cores (see the pair of grains 7/8 with $d = 0.4$ μm, $\Gamma = 15.42$ mm^{-1} at the grain boundary and $2.80 \leqslant \Gamma \leqslant 8.82$ mm^{-1} in the cores of 7 and 8).
- Some pileups formed in large grains vanish in smaller microstructures. This is the case at the grain boundary between 9 and 10, where $\Gamma = 4.51$, 4.47 and 3.61 mm^{-1} for $d = 20$, 4 and 0.4 μm respectively.

The field of Γ is generally localised at the grain boundaries. When the grain size is smaller, this field spreads over the grain cores and affect entire grains. In fact, the strain gradient effects are controlled by the intrinsic length scale, l_s, so that the simulated GND affected zones is directly related to l_s. Then, decreasing the grain size amounts to increasing the relative size of these zones.

The histograms of Fig. 6b confirm the previous observations. The curve obtained for $d = 20$ μm with a high peak for small values of Γ describes a homogeneous distribution where most of the integration points exhibit a low norm of the dislocation density tensor. When d gets smaller, the peak is decreasing and is centered at higher values of Γ. This describes the spreading over the microstructure, leading to an heterogeneous field of Γ. The same distributions are obtained for $d = 1$ μm and $d = 0.4$ μm. As we get closer to l_s, the model starts to saturate as it was shown in Fig. 3. The strain gradients become energetically too expensive and cannot develop so that the field does not evolve anymore.

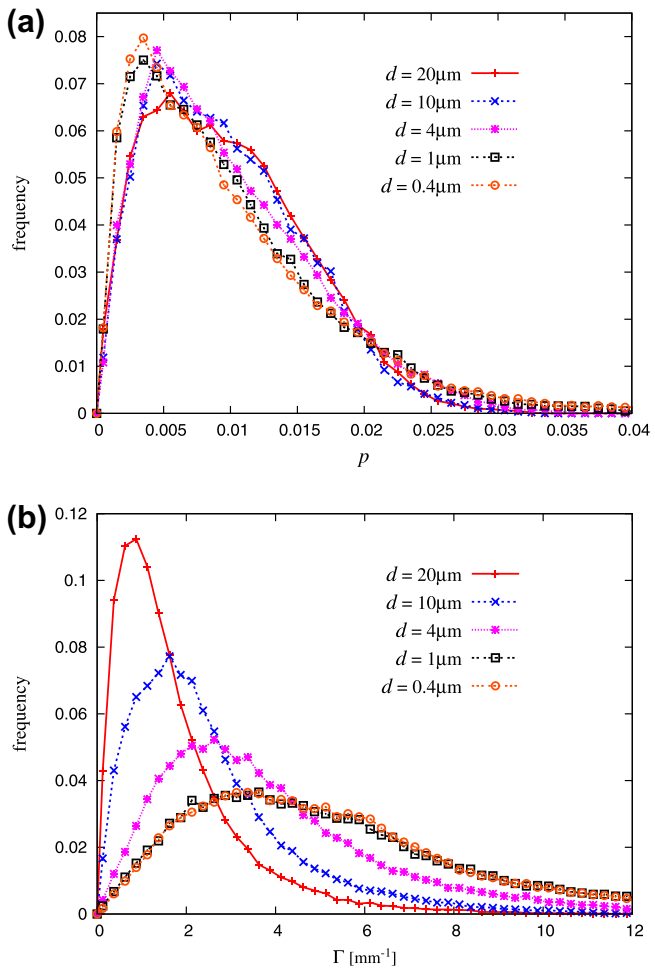

Fig. 6. Distributions of (a) p and (b) Γ in the considered aggregates under simple shear for the same overall value $\langle p \rangle = 0.001$ and for various grain sizes. The frequency represents the fraction of integration points where (a) p takes the value of $p \pm \Delta p$ or (b) Γ takes the value of $\Gamma \pm \Delta\Gamma$. These histograms are obtained by including all the values from the three realisations of the 24-grain aggregate and from the 52-grain aggregate and with interval sizes of $2\Delta p = 0.001$ and $2\Delta\Gamma = 0.25\ \mathrm{mm}^{-1}$.

It is remarkable that the Γ field does not correlate with the plastic strain field. In particular, the network of slip bands observed in Fig. 4 is not systematically associated with high GND densities. This means that the slip bands form without inducing higher lattice curvature in contrast to kink bands sometimes observed in simulations [14]. The following interpretation is proposed. The slip band network that develops in fine grained polycrystals is such that plastic strain is maximised without a significant increase of GND densities. This is possible only for specific relative orientations of grains and leads to a selection of the formed slip bands.

5. Conclusions

Finite element simulations have been performed to investigate the grain size effects in polycrystalline aggregates in generalised continuum crystal plasticity. The *microcurl* model has been chosen for its ability to produce a size-dependent linear kinematic hardening coming from the dislocation density tensor, or equivalently from the GNDs. The overall response of these polycrystals is strongly linked to the size of the microstructure, especially in a size-dependent zone where grain sizes range from 0.4 μm to 20 μm. A strong dependence on the size is also observed on plastic strain and dislocation density tensor fields. A network of strain localisation bands is progressively built and lattice curvature spreads over the grains when the microstructure size is smaller. This slip band network in ultra-fine grains is a new feature of generalised crystal plasticity. The question remains open whether such phenomenon will still occur in the case of 3D simulations with more than 2 slip systems.

On the other hand, the size of the intragranular domains affected by lattice curvature found in the simulations can be used as input to calibrate mean field models with internal length scales as in [25].

Acknowledgement

The authors would like to thank Dr. Laurent Capolungo for his valuable comments and discussions.This work is part of the NANOCRYSTAL project ANR-07-BLAN-0186. Financial support of ANR is gratefully acknowledged.

References

[1] A. Acharya, A.J. Beaudoin, Journal of the Mechanics and Physics of Solids 48 (10) (2000) 2213–2230.
[2] R.J. Asaro, Journal of applied mechanics 50 (1983) 921.
[3] F. Barbe, L. Decker, D. Jeulin, G. Cailletaud, International Journal of Plasticity 17 (2001) 513–536.
[4] S. Bargmann, M. Ekh, K. Runesson, B. Svendsen, Philosophical Magazine 90 (10) (2010) 1263–1288.
[5] C.J. Bayley, W.A.M. Brekelmans, M.G.D. Geers, Philosophical Magazine 87 (2007) 1361–1378.
[6] V.P. Bennett, D.L. McDowell, Engineering Fracture Mechanics 70 (2) (2003) 185–207.
[7] E.P. Busso, F.T. Meissonier, N.P. O'Dowd, Journal of Mechanics and Physics of Solids 48 (11) (2000) 2333–2361.
[8] P. Cermelli, M.E. Gurtin, Journal of the Mechanics and Physics of Solids 49 (2001) 1539–1568.
[9] K.S. Cheong, E.P. Busso, A. Arsenlis, International Journal of Plasticity 21 (2005) 1797–1814.
[10] M. Cherkaoui, L. Capolungo, Atomistic and Continuum Modeling of Nanocrystalline Materials: Deformation Mechanisms and Scale Transition, Springer Verlag, 2009.
[11] N.M. Cordero, S. Forest, E.P. Busso, S. Berbenni, M. Cherkaoui, Grain size effects in generalised continuum crystal plasticity, in: Scale Transition for Plastic Crystalline and Microstructured Materials: From Experiment to Numerical Modeling, ICACM 2010, Hermès, Paris, 2011.
[12] N.M. Cordero, A. Gaubert, S. Forest, E.P. Busso, F. Gallerneau, S. Kruch, Journal of the Mechanics and Physics of Solids 58 (2010) 1963–1994.
[13] A.C. Eringen, Microcontinuum Field Theories, Springer, New York, 1999.
[14] S. Forest, Acta Materialia 46 (9) (1998) 3265–3281.
[15] S. Forest, Journal of Engineering Mechanics 135 (2009) 117–131.
[16] S. Forest, F. Barbe, G. Cailletaud, International Journal of Solids and Structures 37 (2000) 7105–7126.
[17] S. Forest, F. Pradel, K. Sab, International Journal of Solids and Structures 38 (2001) 4585–4608.
[18] S. Forest, R. Sedláček, Philosophical Magazine A 83 (2003) 245–276.
[19] M.E. Gurtin, Journal of the Mechanics and Physics of Solids 50 (2002) 5–32.
[20] M.E. Gurtin, L. Anand, Journal of the Mechanics and Physics of Solids 56 (2008) 184–199.
[21] L. Méric, G. Cailletaud, M. Gaspérini, Acta Metallurgica Et Materialia 42 (1994) 921–935.
[22] D.P. Mika, P.R. Dawson, Materials Science and Engineering A 257 (1998) 62–76.
[23] J.F. Nye, Acta Metallurgica 1 (1953) 153–162.
[24] C. Perrin, S. Berbenni, H. Vehoff, M. Berveiller, Acta Materialia 58 (14) (2010) 4639–4649.
[25] J.M. Pipard, N. Nicaise, S. Berbenni, O. Bouaziz, M. Berveiller, Computational Materials Science 45 (3) (2009) 604–610.
[26] P.G. Sanders, J.A. Eastman, J.R. Weertman, Acta Materialia 45 (10) (1997) 4019–4025.
[27] L. St-Pierre, E. Héripré, M. Dexet, J. Crépin, G. Bertolino, N. Bilger, International Journal of Plasticity 24 (2008) 1516–1532.
[28] Y.M. Wang, K. Wang, D. Pan, K. Lu, K.J. Hemker, E. Ma, Scripta Materialia 48 (12) (2003) 1581–1586.
[29] A. Zeghadi, S. Forest, A.F. Gourgues, O. Bouaziz, Philosophical Magazine 87 (2007) 1425–1446.